CrossMark

Search for the Metal-weak Thick Disk from the LAMOST DR5

Tai-Sheng Yan[1,2] , Jian-Rong Shi[1,2] , Hao Tian[3] , Wei Zhang[1] , and Bo Zhang[4]

[1] Key Laboratory of Optical Astronomy, National Astronomical Observatories, Chinese Academy of Sciences, Beijing 100012, China; sjr@bao.ac.cn
[2] School of Astronomy and Space Science, University of Chinese Academy of Sciences, Beijing 100049, China
[3] Key Laboratory of Space Astronomy and Technology, National Astronomical Observatories, Chinese Academy of Sciences, Beijing 100101, China
tianhao@nao.cas.cn
[4] Department of Astronomy, Beijing Normal University, Beijing 100875, China

Abstract

Based on the data release of the Large Sky Area Multi-Object Fiber Spectroscopic Telescope survey (LAMOST DR5) and the Gaia Early Data Release 3 (Gaia EDR3), we construct a sample containing 46,109 giant ($\log g \leqslant 3.5$ dex) stars with heliocentric distance $d \leqslant 4$ kpc, and the sample is further divided into two groups of the inner ($R_{GC} < 8.34$ kpc) and outer region ($R_{GC} > 8.34$ kpc). The L_Z distributions of our program stars in the panels with different [Fe/H] and [α/Fe] suggest that the thick-disk consists of two distinct components with different chemical compositions and kinematic properties. For the inner region, the metal-weak thick disk (MWTD) significantly contributes when [α/Fe] > +0.2 dex and [Fe/H] < −0.8 dex, while the canonical thick-disk (TD) dominates when [Fe/H] > −0.8 dex. However, MWTD clearly appears only when [α/Fe] > +0.2 dex and [Fe/H] < −1.2 dex for the outer region, and its proportion is lower than that of the inner region within the same metallicity. Similar results can be obtained from the V_ϕ distribution. The higher fraction of MWTD in the inner region than that in the outer region implies that MWTD may form in the inner disk, and is observational evidence about the inside-out disk formation scenario.

Key words: stars: abundances – stars: atmospheres – Galaxy: structure – Galaxy: kinematics and dynamics – methods: data analysis

1. Introduction

It is well known that the Milky Way is composed of multiple components, such as the thin-disk, the thick-disk and the halo (Chiappini et al. 1997; van der Kruit & Freeman 2011; An & Beers 2020), and it provides a unique chance for studying the formation and evolution of galaxies in detail by analyzing the full location, kinematics characteristic and chemical compositions of these stellar components.

As an important component of our Galaxy, the thick-disk has been studied by numerous works since its discovery (Gilmore & Reid 1983; Girard et al. 2006; Di Matteo et al. 2011; Ruchti et al. 2011; Recio-Blanco et al. 2014; Helmi et al. 2018; Di Matteo et al. 2019; Beraldo e Silva et al. 2021; Franchini et al. 2021). The thick-disk is primarily composed of older stars, resulting in different chemical composition from the young thin-disk stars. In the metallicity distribution, the thick-disk exhibits a peak aound [Fe/H] = −0.6 dex, and most of the thick-disk stars fall within the interval of [Fe/H] from −1.0 dex to −0.3 dex (Reddy & Lambert 2008). At the moment, there is no uniform conclusion on the upper and lower bounds of the metallicity distribution for the thick-disk stars (Reddy & Lambert 2008), and some disk-like kinematics stars with very low metallicity (down to [Fe/H] = −1.7 dex, or even lower) have been found (Norris et al. 1985; Chiba & Beers 2000;

Carollo et al. 2010, 2019). These metal-poor tail stars are commonly considered to belong to the metal-weak thick-disk (MWTD, Morrison et al. 1990; Ivezić et al. 2008; Reddy & Lambert 2008; Carollo et al. 2010; Ruchti et al. 2011; Beers et al. 2014; Carollo et al. 2019; Carollo & Chiba 2021), while the remaining component after removing MWTD from the thick-disk is called as the canonical thick-disk (TD, Carollo et al. 2010).

Due to lack of large-scale sample stars of high-precision parameters, the existence of MWTD remains controversial (Ruchti et al. 2010). Norris et al. (1985) suggested that these stars with [Fe/H] ⩽ −1.0 dex and $e \leqslant 0.4$ should belong to a population, and Morrison et al. (1990) referred to these stars of −1.6 dex < [Fe/H] < −1.0 dex with kinematical and spatial properties similar to the thick-disk ones as MWTD stars. It need to be pointed out that the metallicity derived by Norris et al. (1985) and Morrison et al. (1990) is based on the information from the David Dunlap Observatory (DDO) photometry, and Twarog & Anthony-Twarog (1994) found that the photometric metallicity used by Norris et al. (1985) has an ∼0.5 dex offset from the spectral ones for giants near [Fe/H] ∼ −1.2 dex. In addition, by comparing the metallicity obtained from the high-resolution spectra with these from the DDO photometry for giants of Norris et al. (1985) and

Morrison et al. (1990); Ryan & Lambert (1995) concluded that most stars with the DDO photometric metallicity of [Fe/H] < −1.0 dex have spectral metallicities of [Fe/H] > −1.0 dex. As a result, these stars identified as belonging to MWTD by Norris et al. (1985) and Morrison et al. (1990), therefore should belong to TD. Although the conclusions from Twarog & Anthony-Twarog (1994) and Ryan & Lambert (1995) cannot rule out the existence of MWTD, the evidence of MWTD suggested by Norris et al. (1985) and Morrison et al. (1990) becomes weaker.

Fortunately, the advent of large-scale surveys, such as the Large Sky Area Multi-Object Fiber Spectroscopic Telescope (LAMOST) survey (Cui et al. 2012), the Sloan Digital Sky Survey (SDSS, York et al. 2000), the Radial Velocity Experiment spectroscopic survey (RAVE, Steinmetz et al. 2020a, 2020b), and the Gaia mission (Gaia Collaboration et al. 2021), make it possible to perform accurate chemodynamical studies on the stellar populations in our Galaxy (Carollo et al. 2019). The spectra from LAMOST, SDSS and RAVE provide estimation of the stellar atmospheric parameters (effective temperature, surface gravity and metallicity) and radial velocities (RV), and the Gaia satellite delivers high-precision astrometric data (position, trigonometric parallax, and proper motions). The combination of parameters obtained from spectrum and astrometry is a powerful tool for studying the properties of stellar component related to the Milky Way by investigating the perspectives of stellar spatial distribution, chemical composition and kinematics.

In this paper, based on a sample combining spectral information from LAMOST and astrometric data from Gaia, we examine MWTD. The paper is organized as follows. In Section 2, we describe the selection of our sample stars. Section 3 presents the search for MWTD in the kinematic space, and the discussion and conclusions are given in Section 4.

2. Sample

2.1. Selection of the Sample Stars

The sample stars are selected from LAMOST DR5 with a range of the effective temperature from 4500 to 7000 K, and only the giants (log $g \leqslant 3.5$ dex) with signal-to-noise ratio (S/N) of their spectra higher than 50 have been considered. This removes all the dwarf stars. The stellar atmosphere parameters and [α/Fe] ratios are taken from the recommended values of Xiang et al. (2019) with internal uncertainties of [Fe/H] and [α/Fe] less than 0.07 and 0.05 dex, respectively, while the RVs are adopted from LAMOST DR5 (Luo et al. 2015), and only the objects with an RV uncertainty less than 10 km s^{-1} have been selected. Moreover, to further ensure the accuracy of the metallicity, only the objects with a difference of metallicity between LAMOST DR5 and that of Xiang et al. (2019) less than 0.1 dex are selected.

The stellar proper motions (PMs) are obtained from Gaia EDR3 (Gaia Collaboration et al. 2021) with errors both in R.A.
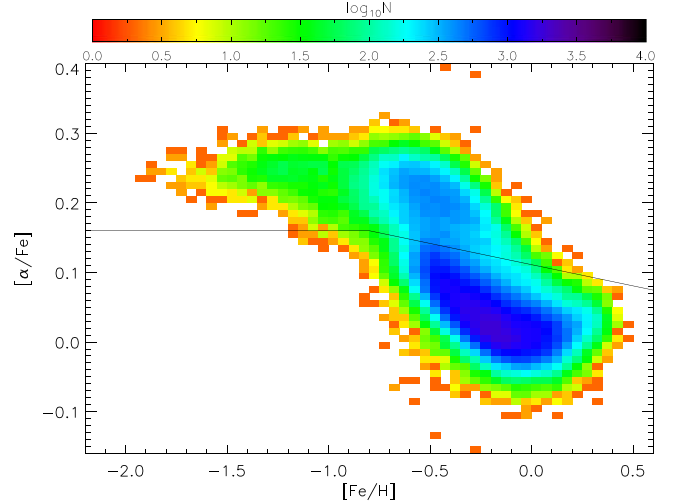

Figure 1. Distribution of giant stars in the [α/Fe]–[Fe/H] plane. The black yellow polyline is the criteria for dividing the thin- and thick-disk stars from Hayden et al. (2014).

and in decl. direction less than 0.2 mas yr^{-1}, while the geometric distances ($r_{\rm med}$) from Bailer-Jones et al. (2021) have been adopted. Our sample stars are confined to d ⩽ 4 kpc with an uncertainty of ($r_{\rm hi} - r_{\rm lo})/(2 \times r_{\rm med})$ smaller than 20%. Here, $r_{\rm lo}$ and $r_{\rm hi}$ are the 16th and 84th percentiles of the posterior (see Bailer-Jones et al. 2021, for details).

After these considerations included, the number of stars is reduced to 211,046, and the distribution of these stars in the [α/Fe]–[Fe/H] plane is shown in Figure 1. Obviously, most of them are belong to the thin-disk, and these thin-disk stars are not important for this study. Therefore, according to the criteria of Hayden et al. (2014) (see the black yellow polyline in Figure 1) we remove them from our sample. Finally, there are 46,109 stars in our sample.

To avoid the systematic offset of LAMOST RVs (Anguiano et al. 2018; Tian et al. 2020), we compare the LAMOST RVs with those from Gaia EDR3 for the common stars, only stars with Gaia RV errors less than 1 km s^{-1} have been selected. The offset of LAMOST RV is around −4.85 km s^{-1} (Figure 2), which is very close to those of the previous works (∼−5 km s^{-1}, Anguiano et al. 2018; Tian et al. 2020). Therefore, a value of 4.85 km s^{-1} is added to the LAMOST RV to compensate for the offset.

2.2. Stellar Kinematic Parameters

The full phase-space information, positions (including α, δ and l, b), PMs and distances, combined with RVs, provide the parameters required to calculate the kinematics. Following Kordopatis et al. (2011), the Galactic-centerd Cartesian coordinates ($X_{\rm GC}$, $Y_{\rm GC}$, $Z_{\rm GC}$) of stars are obtained through their distances and Galactic coordinates (l, b), and $R_{\rm GC} = \sqrt{X_{\rm GC}^2 + Y_{\rm GC}^2}$
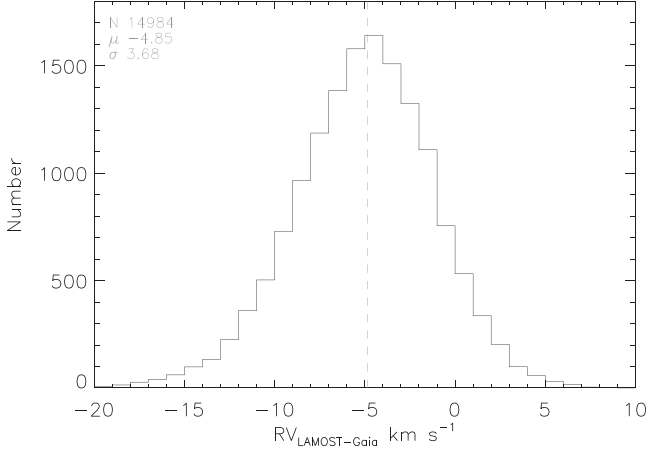
Figure 2. Comparison of the LAMOST RVs with those from Gaia EDR3, only stars with Gaia RV errors less than 1 km s^{-1} have been used.

Figure 3. [α/Fe] distribution of the sample stars with [Fe/H] < −0.8 dex. The distribution can be well fitted with two Gaussian components. The vertical dotted line is labeled as [α/Fe] = +0.2 dex.

represents the distance to the Galactic center in planar radial coordinate. In our calculation, the solar position of $(X_\odot, Y_\odot, Z_\odot) = (8.34$ kpc, 0, 0) is adopted (Reid et al. 2014). The galactocentric velocities V_R and V_ϕ are also calculated, and V_R and V_ϕ are defined as positive with increasing R_{GC} and ϕ, respectively. The Galactic rotation velocity of the local standard of rest (LSR) is adopted as $V_c = 240$ km s^{-1} (Reid et al. 2014), and the solar motion with respected to LSR of $(U_\odot, V_\odot, W_\odot) = (11.1, 12.24, 7.25)$km s^{-1}, is taken from Schönrich et al. (2010). The Z-axis angular momentum is derived using the relationship of $L_Z = R_{GC} \times V_\phi$.

3. Results

Although MWTD overlaps TD and the halo in parameter space, it is still possible to trace the footprint of MWTD with the help of their distribution in the metallicities, kinematics and dynamics (Carollo et al. 2010; Kordopatis et al. 2013; Carollo et al. 2019; An & Beers 2020, 2021; Carollo & Chiba 2021; Cordoni et al. 2021).

It is noted that the fraction of metal-poor stars is lower (see Figure 8 of Miranda et al. 2016), and Carollo et al. (2010) pointed out that the significant contribution of MWTD is within −1.8 dex < [Fe/H] < −0.8 dex, and possibly up to ∼−0.7 dex. Therefore, we divide our sample stars into four metallicity intervals of [Fe/H] < −1.2 dex, −1.2 dex < [Fe/H] < −0.8 dex, −0.8 dex < [Fe/H] < −0.4 dex and [Fe/H] > −0.4 dex. Moreover, Carollo et al. (2019) suggested that the MWTD stars tend to have higher [α/Fe] ratios than those of TD, which means it will improve the search efficiency of MWTD when the sample is decomposed in [α/Fe] space. In Figure 3 we plot the [α/Fe] distribution of our sample stars of [Fe/H] < −0.8 dex, and the distribution can be well fitted with two Gaussian functions. According to their [α/Fe] distribution, the sample is further
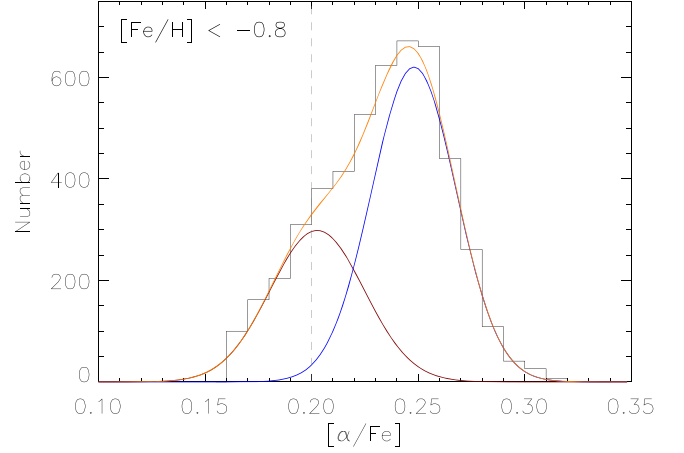
divided into high ([α/Fe] > +0.2 dex) and low α ([α/Fe] < +0.2 dex) intervals.

In order to compare the differences due to different R_{GC} (e.g., An & Beers 2021), we present our discussions on our program stars with the inner (R_{GC} < 8.34, 23,664 stars) and outer (R_{GC} > 8.34 kpc, 22,445 stars) regions.

3.1. The L$_Z$ Distributions

Following Carollo et al. (2019), we focus on the L_Z distribution. In Figure 4, we plot the L_Z distribution for the inner region stars (R_{GC} < 8.34) in slices of [Fe/H] and [α/Fe]. We apply multi-Gaussians to fit the L_Z distribution in each panel, and the fitting parameters of each component including the fraction, L_Z and scatter (σ_{LZ}) are derived according to the Bayesian method, which can effectively avoid the contamination between different components (Tian et al. 2019). To perform this fitting, we apply *emcee* (Foreman-Mackey et al. 2013) to run a Markov Chain Monte Carlo (MCMC) simulation. We use 100 walkers for 2000 iterations with 1000 burn-in have been used. The median value for each parameter is adopted, and the difference between the median value and the 16% and 84% values are used as the upper and lower uncertainties, respectively. Figure 5 shows the MCMC result of panel (b) in Figure 4.

The best-fit parameters and uncertainties of the MCMC simulations for all the subsamples are listed in Table 1. When the fraction is not a free parameter during the MCMC simulation (one in each panel), its uncertainty is marked as 0 (Table 1). The fitted distributions are represented with brown, red, green and blue lines for the halo, MWTD, TD and total, respectively, in Figure 4.

It can be seen from Figure 4 that the three low α ([α/Fe] < +0.20 dex) panels ((f), (g) and (h)) are dominated by the TD stars, and their L_Z peaks gradually decrease with decreasing

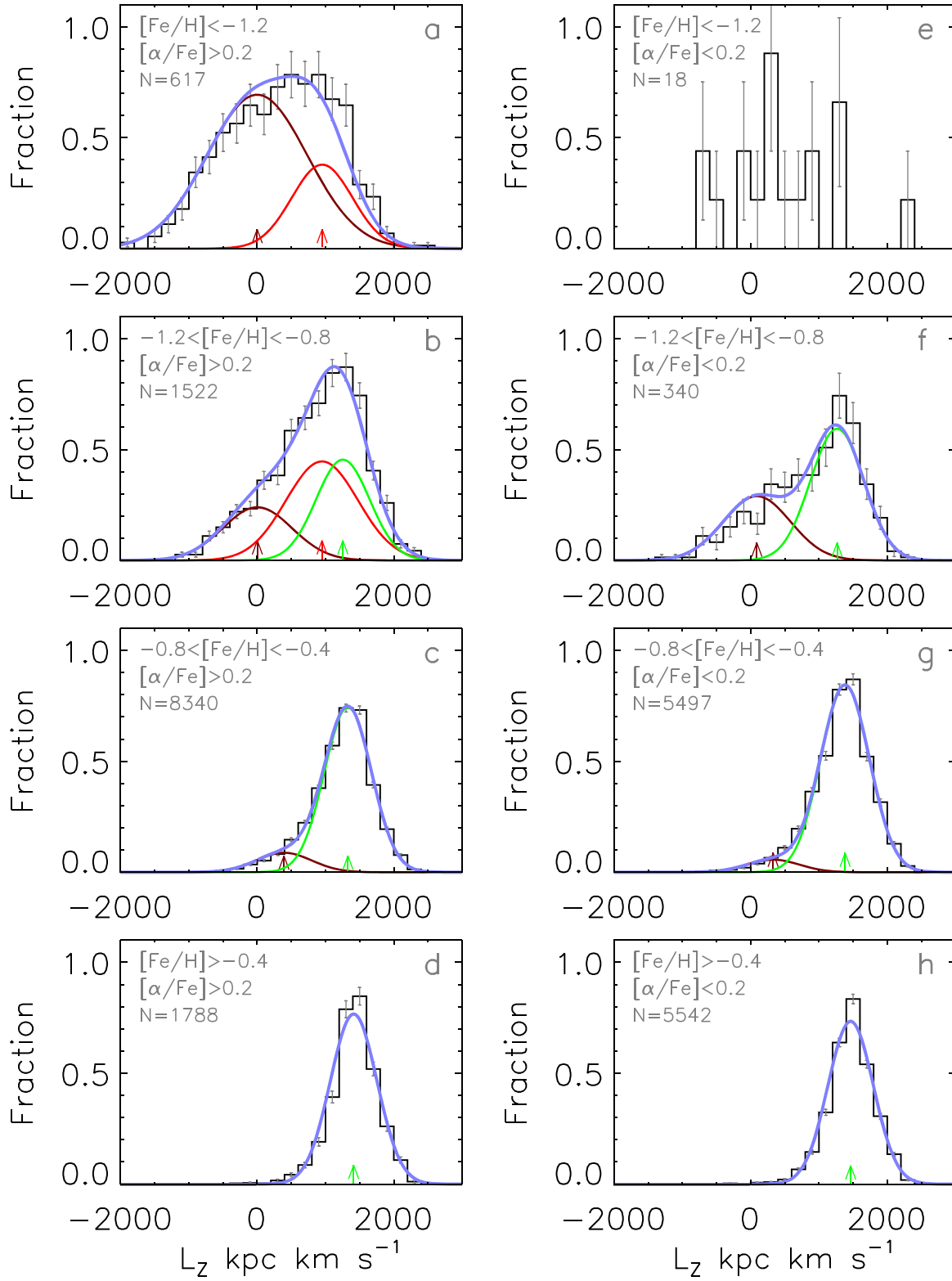**Figure 4.** The L_Z distributions of the inner region stars in slices of [Fe/H] and [α/Fe]. The distribution can be best-fitted by one to three Gaussian(s), and each represents one component: the halo (brown), MWTD (red) and TD (green). The black histogram is the sum of all stars, while the light blue solid line represents the sum of the fit components.
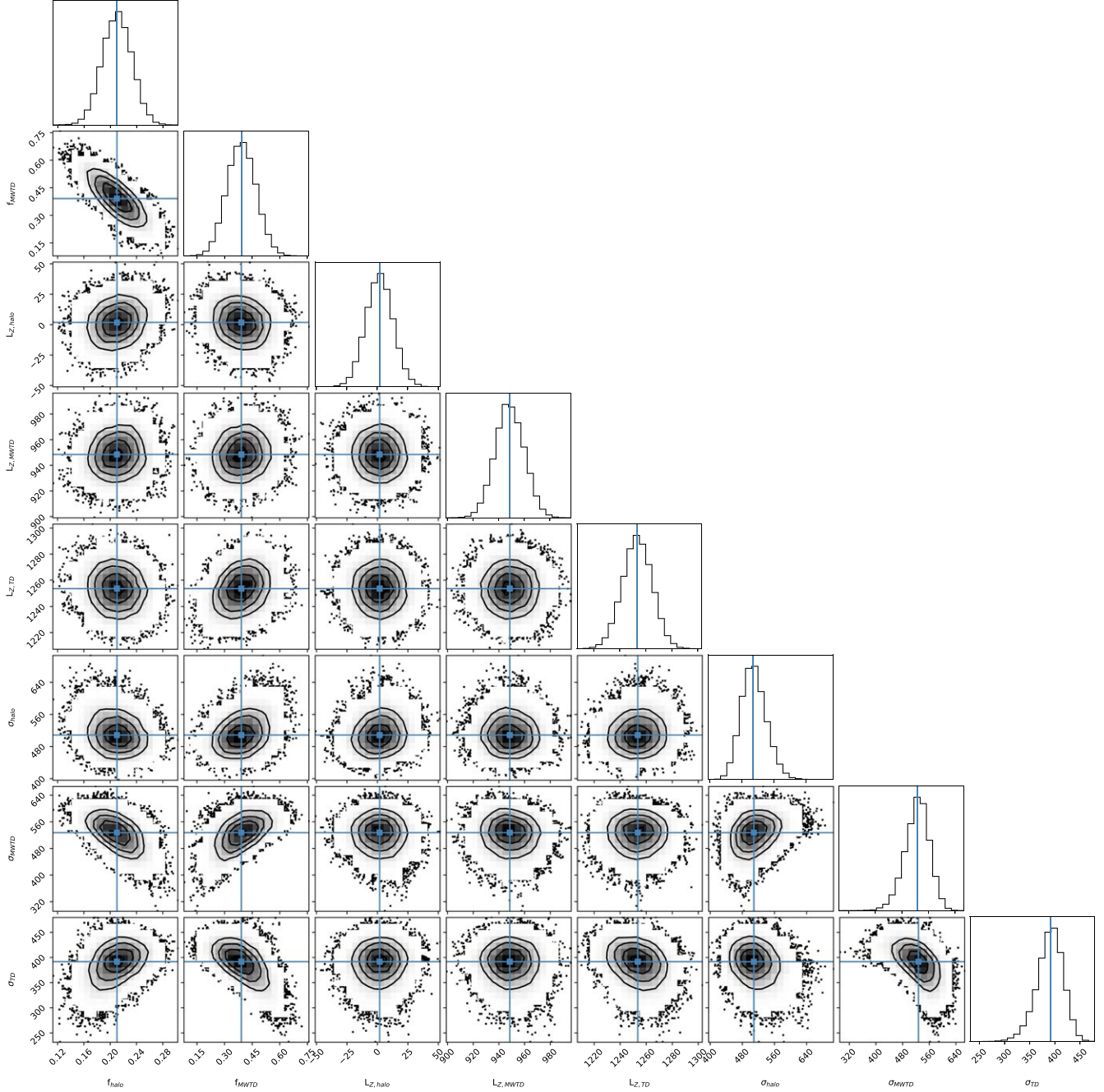
Figure 5. The MCMC simulation results of panel (b) of Figure 4. The adopted median values of the parameters are represented by the solid blue lines.

metallicity. When $[Fe/H] < -0.4$ dex, the halo exists (panels (f) and (g)), and it accounts for about one third when -1.2 dex $< [Fe/H] < -0.8$ dex (panel (f)).

For the four high α panels, the L_Z distributions vary regularly with the metallicity. The TD stars dominate both in panels (c) and (d), and the L_Z distribution of these two panels are very similar to those of panels (g) and (h). The typical L_Z peak value is around 1350 kpc km s^{-1}.

We note that there are three components in panel (b), and one of them has a L_Z peak of 948.5 ± 11.2 kpc km s^{-1} with a scatter of 527.5 ± 37.0 kpc km s^{-1}, this value is lower than that of TD (1253.5 ± 11.3 kpc km s^{-1}), while it is higher than that of the halo (1.8 ± 11.2 kpc km s^{-1}). This indicates that this component is dynamically different from those of the halo and TD, and it is most likely to be MWTD (Carollo et al. 2010; An & Beers 2020; Naidu et al. 2020). The difference of the L_Z

Table 1
The Parameters of the Best-fit Components in the L_Z Distributions for the Inner Region Stars in Slices of [Fe/H] and [α/Fe]

[α/Fe]	Component	[Fe/H] < −1.2 dex			−1.2 dex < [Fe/H] < −0.8 dex			−0.8 dex < [Fe/H] < −0.4 dex			[Fe/H] > −0.4 dex		
		Fraction	L_Z peak	σ_{LZ}	Fraction	L_Z peak	σ_{LZ}	Fraction	L_Z peak	σ_{LZ}	Fraction	L_Z peak	σ_{LZ}
>0.2	TD				0.40 ± 0	1253.5 ± 11.3	391.6 ± 26.4	0.89 ± 0	1328.2 ± 7.1	346.1 ± 5.0	1.00 ± 0	1412.0 ± 8.0	341.3 ± 5.9
	MWTD	0.35 ± 0	950.7 ± 7.0	444.9 ± 35.4	0.39 ± 0.08	948.5 ± 11.2	527.5 ± 37.0						
	the halo	0.65 ± 0.03	−0.2 ± 7.1	733.6 ± 33.6	0.21 ± 0.02	1.8 ± 11.2	508.8 ± 31.5	0.11 ± 0.01	391.6 ± 41.5	405.2 ± 18.8			
<0.2	TD				0.67 ± 0	1265.3 ± 40.8	390.0 ± 33.7	0.94 ± 0	1383.1 ± 7.2	356.2 ± 5.5	1.00 ± 0	1464.0 ± 4.5	331.6 ± 3.3
	the halo				0.33 ± 0.05	91.2 ± 61.4	490.6 ± 50.1	0.06 ± 0.01	329.6 ± 48.1	384.9 ± 23.8			

Note. The units of the L_Z peak and scatter (σ_{LZ}) are in kpc km s^{-1}.
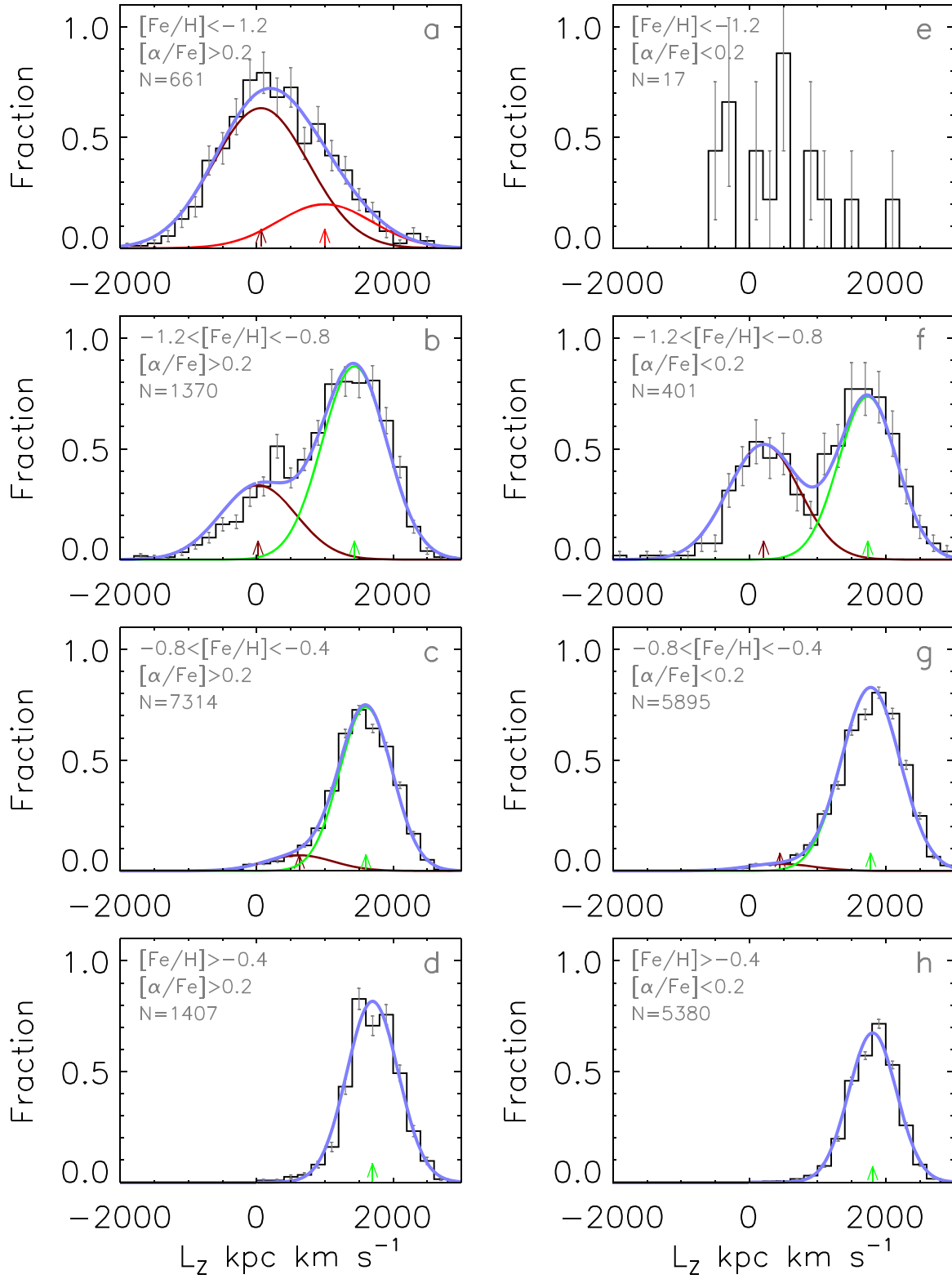
Figure 6. Similar to Figure 4 but for the L_Z distribution of outer region stars.

Table 2
Similar to Table 1, but for the Outer Region Stars

| $[\alpha/Fe]$	Component	[Fe/H] < −1.2			−1.2 < [Fe/H] < −0.8			−0.8 < [Fe/H] < −0.4			[Fe/H] > −0.4		
		Fraction	L_Z peak	σ_{LZ}	Fraction	L_Z peak	σ_{LZ}	Fraction	L_Z peak	σ_{LZ}	Fraction	L_Z peak	σ_{LZ}
>0.2	TD				0.72 ± 0	1432.5 ± 12.8	475.6 ± 15.0	0.91 ± 0	1600.4 ± 10.5	386.8 ± 6.4	1.00 ± 0	1697.4 ± 10.2	378.7 ± 7.3
	MWTD	0.24 ± 0	996.9 ± 22.0	687.8 ± 62.1									
	the halo	0.76 ± 0.04	60.8 ± 21.9	701.4 ± 30.2	0.28 ± 0.02	19.1 ± 15.2	555.4 ± 28.1	0.09 ± 0.02	625.3 ± 136.6	494.0 ± 55.2			
<0.2	TD				0.59 ± 0	1736.4 ± 44.1	427.2 ± 30.1	0.96 ± 0	1779.6 ± 49.8	427.9 ± 14.2	1.00 ± 0	1808.0 ± 4.8	350.2 ± 3.4
	the halo				0.41 ± 0.04	211.3 ± 86.7	525.5 ± 62.6	0.04 ± 0.01	450.4 ± 30.1	485.2 ± 35.8			
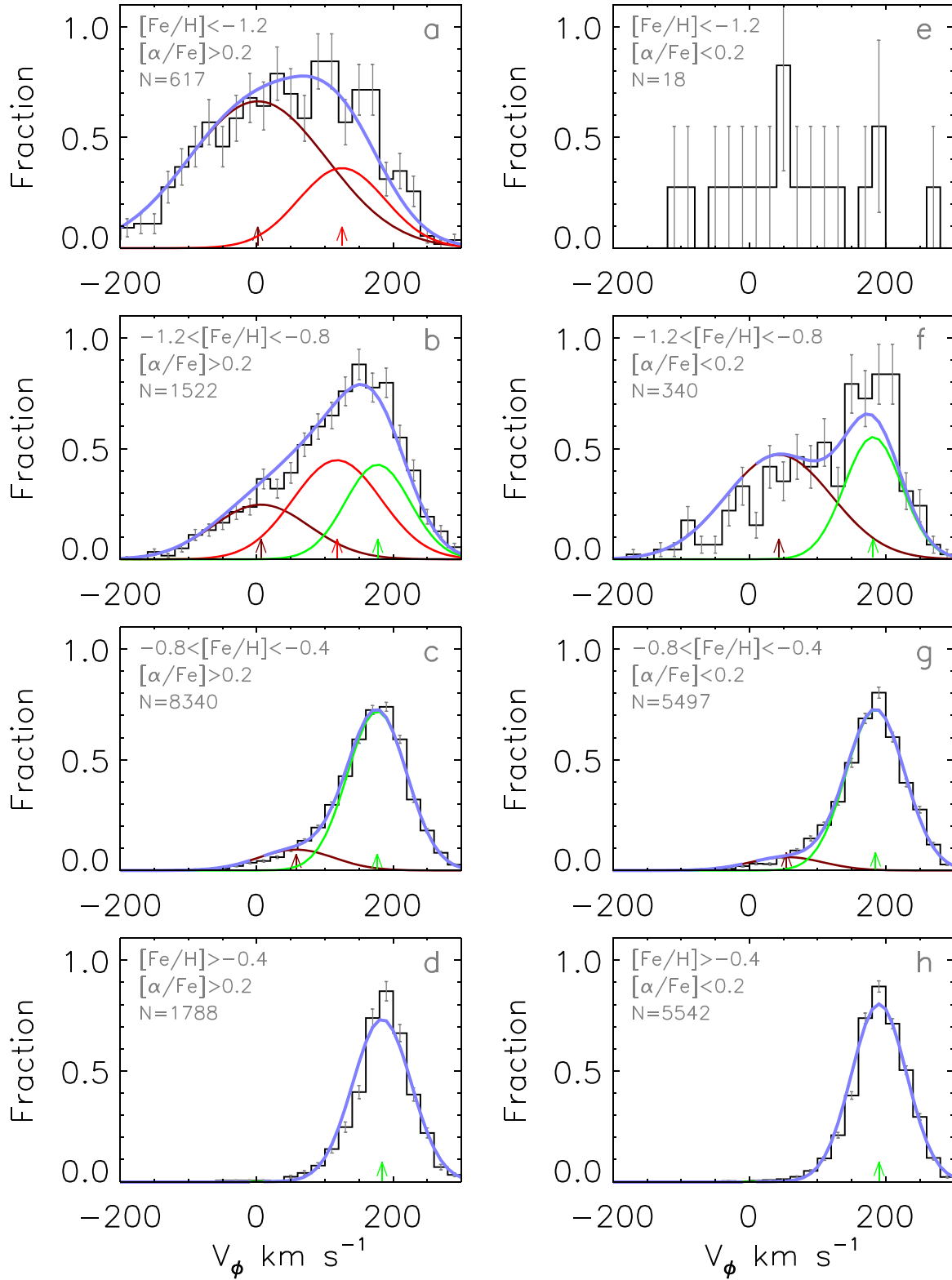
Figure 7. Similar to Figure 4 but for the V_ϕ distribution.
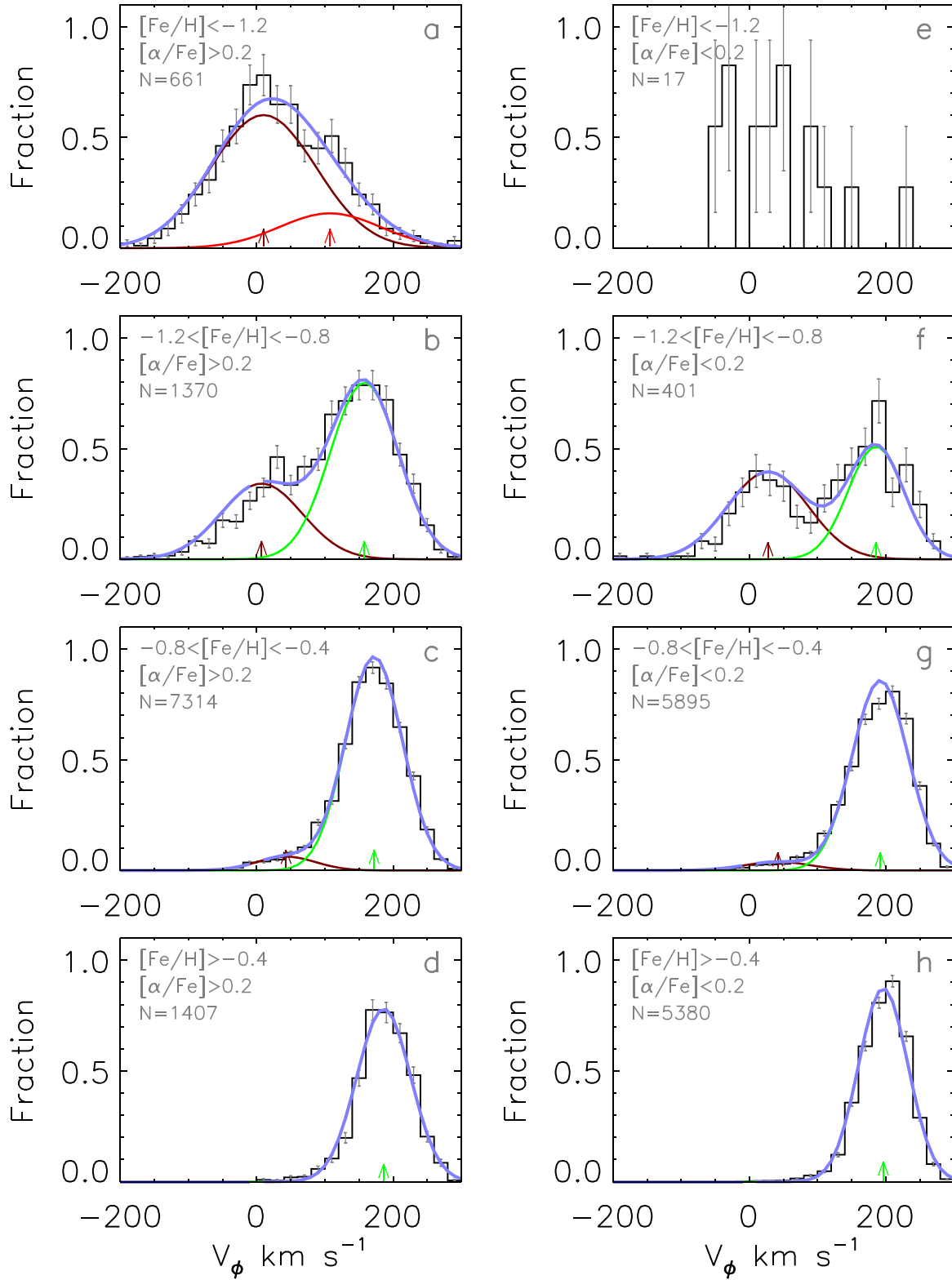
Figure 8. Similar to Figure 7 but for the outer stars ($R_{GC} > 8.34$ kpc).

Table 3
The Parameters of the Best-fit Components in the V_ϕ Distributions for Inner Region Stars ($R_{GC} < 8.34$ kpc)

[α/Fe]	Component	[Fe/H] < −1.2			−1.2 < [Fe/H] < −0.8			−0.8 < [Fe/H] < −0.4			[Fe/H] > −0.4		
		Fraction	V_ϕ peak	$\sigma_{V\phi}$	Fraction	V_ϕ peak	$\sigma_{V\phi}$	Fraction	V_ϕ peak	$\sigma_{V\phi}$	Fraction	V_ϕ peak	$\sigma_{V\phi}$
>0.2	TD				0.38 ± 0	177.4 ± 7.2	47.6 ± 3.9	0.88 ± 0	176.5 ± 0.9	43.6 ± 0.6	1.00 ± 0	183.7 ± 1.0	42.9 ± 0.7
	MWTD	0.35 ± 0	124.9 ± 6.3	63.4 ± 6.5	0.40 ± 0.12	117.8 ± 10.7	64.6 ± 8.8						
	the halo	0.65 ± 0.05	1.4 ± 6.8	101.6 ± 5.5	0.22 ± 0.05	6.2 ± 10.6	71.2 ± 6.2	0.12 ± 0.01	57.8 ± 6.0	55.9 ± 2.6			
<0.2	TD				0.54 ± 0	181.5 ± 6.4	42.0 ± 5.3	0.92 ± 0	185.0 ± 0.9	43.0 ± 0.7	1.00 ± 0	190.2 ± 0.5	40.4 ± 0.4
	the halo				0.46 ± 0.08	43.3 ± 14.9	77.4 ± 8.2	0.08 ± 0.01	54.6 ± 6.4	53.7 ± 3.1			

Note. The units of $\langle V_\phi \rangle$ and $\sigma_{V\phi}$ are in km s^{-1}.

Table 4
Similar to Table 3 but for the V_ϕ Distributions of Outer Region Stars ($R_{GC} > 8.34$ kpc)

$[\alpha/\mathrm{Fe}]$	Component	$[\mathrm{Fe/H}] < -1.2$			$-1.2 < [\mathrm{Fe/H}] < -0.8$			$-0.8 < [\mathrm{Fe/H}] < -0.4$			$[\mathrm{Fe/H}] > -0.4$		
		Fraction	V_ϕ peak	$\sigma_{V\phi}$	Fraction	V_ϕ peak	$\sigma_{V\phi}$	Fraction	V_ϕ peak	$\sigma_{V\phi}$	Fraction	V_ϕ peak	$\sigma_{V\phi}$
>0.2	TD				0.70 ± 0	157.7 ± 1.9	49.8 ± 1.7	0.94 ± 0	172.1 ± 0.7	41.6 ± 0.5	1.00 ± 0	186.2 ± 1.1	39.6 ± 0.8
	MWTD	0.21 ± 0	107.4 ± 7.1	74.3 ± 20.7									
	the halo	0.79 ± 0.07	10.0 ± 6.9	77.2 ± 4.0	0.30 ± 0.02	7.0 ± 2.8	59.5 ± 3.0	0.06 ± 0.01	43.0 ± 5.5	43.0 ± 2.9			
<0.2	TD				0.56 ± 0	185.6 ± 4.2	40.9 ± 2.9	0.96 ± 0	191.9 ± 0.6	40.9 ± 0.5	1.00 ± 0	196.4 ± 0.5	36.1 ± 0.4
	the halo				0.44 ± 0.04	27.2 ± 8.5	59.2 ± 6.4	0.04 ± 0	41.7 ± 5.1	48.9 ± 3.2			

peak between MWTD and TD is around 300 kpc km s^{-1}, which is larger than that of the fitting error. Our results present that the fraction of MWTD in this panel is around 0.39, while the fractions of the halo and TD are ∼0.21 and ∼0.40, respectively.

For the more metal-poor panel (a), although there are only two components, we notice that there is a component with a L_Z peak of 950.7 ± 7.0 kpc km s^{-1} with a scatter of 444.9 ± 35.4 kpc km s^{-1}. This L_Z peak value is very close to that of MWTD in panel (b), which indicates this component is also MWTD. The contribution of MWTD in this panel is about one third (0.35). The remaining contribution in the panel accounts for about two-thirds, and they come from the halo of an L_Z peak of −0.2 ± 7.1 kpc km s^{-1} with a sctter of 733.6 ± 33.6 kpc km s^{-1}.

Figure 6 presents the L_Z distributions of the outer region stars ($R_{GC} > 8.34$ kpc, black histogram) in slices of [Fe/H] and [α/Fe]. Similar to the inner region, we apply *emcee* to perform an MCMC simulation to determine the components contained of each panel for the outer region stars. The best-fit components obtained through the simulation are superimposed on the histogram of Figure 6 with color curves, and the best-fit parameters are listed in Table 2.

MWTD has obvious contribution only in panel (a) of Figure 6. The fraction of MWTD in this panel is 0.24, which is lower than that in the same panel of the inner region. The L_Z peak of MWTD in this panel is 996.9 ± 22.0 kpc km s^{-1} with a scatter of 687.8 ± 62.1 kpc km s^{-1}, and we note that this scatter is larger than that of the inner ones (∼500 kpc km s^{-1}). The reason is most likely due to the fraction of MWTD in the outer region is lower than that in the inner one.

3.2. The V_ϕ Distributions

It is noted by An & Beers (2021), Carollo et al. (2010) and Kordopatis et al. (2013) that MWTD has kinematic properties different from those of the halo and TD, thus, we display the V_ϕ distribution of the inner and outer region stars in Figures 7 and 8 in slices of [Fe/H] and [α/Fe], respectively. The best-fit result obtained with the MCMC simulation are superimposed on the histogram with color curves, and the best-fit parameters are listed in Tables 3 and 4.

In each panel of the two figures (Figures 7 and 8), the components determined from the V_ϕ distribution are very similar to those from the L_Z ones. The V_ϕ peak of MWTD in panels (a) and (b) of the inner region are 124.9 ± 6.3 km s^{-1} and 117.8 ± 10.7 km s^{-1}, respectively, while it is 107.4 ± 7.1 km s^{-1} in panel (a) of the outer region, which are consistent with those of Carollo et al. (2010) and Kordopatis et al. (2013), however, they are around 15 km s^{-1} lower than those of An & Beers (2021). We note that the matallicites for the sapmle stars of An & Beers (2021) were estimated from the photometric data, while the V_ϕ of their individual stars were computed using photometric distances and proper-motion measurements from

Gaia EDR3, and their sample restricts to stars within ±30° from the Galactic prime meridian. Therefore, the difference in V_ϕ may be due to the different in sample stars.

4. Discussion and Conclusions

Based on the combined data set of LAMOST DR5 and Gaia EDR3, we investigate the kinematic properties of the giant stars in the solar neighborhood. Our results show that MWTD occupies a significant fraction with metallicity lower than −0.8 and [α/Fe] > +0.2 dex. It is found that the fraction of MWTD is significantly higher within the solar orbit radius, while the Z-axis angular momentum is similar to both subsamples divided by the solar orbit radius, 950 and 1000 kpc km s^{-1} for the inner and outer region, respectively. The high fraction of MWTD in the inner solar orbit radius and higher α element abundances may suggest that the MWTD stars were born in the inner region of the primordial disk, and some of them migrated to larger radii, or MWTD is the result of inside out scenario. However, the number of the MWTD stars is relatively small compared to the TD and halo ones, thus, it is hard to make an ascertained estimation of the origin of MWTD under the current situations. To figure out the origin of MWTD, additional constraints from both observations (such as the abundances of C, N, O, Mg, Si, Ca and Ti, etc) and numerical simulations are necessary.

ORCID iDs

Tai-Sheng Yan, ● https://orcid.org/0000-0003-2318-9013
Jian-Rong Shi, ● https://orcid.org/0000-0002-0349-7839
Hao Tian ● https://orcid.org/0000-0003-3347-7596
Wei Zhang ● https://orcid.org/0000-0002-1783-957X
Bo Zhang ● https://orcid.org/0000-0002-6434-7201

References

An, D., & Beers, T. C. 2020, ApJ, 897, 39
An, D., & Beers, T. C. 2021, ApJ, 918, 74
Anguiano, B., Majewski, S. R., Allende Prieto, C., et al. 2018, A&A, 620, A76
Bailer-Jones, C. A. L., Rybizki, J., Fouesneau, M., Demleitner, M., & Andrae, R. 2021, AJ, 161, 147
Beers, T. C., Norris, J. E., Placco, V. M., et al. 2014, ApJ, 794, 58
Beraldo e Silva, L., Debattista, V. P., Nidever, D., Amarante, J. A. S., & Garver, B. 2021, MNRAS, 502, 260
Carollo, D., Beers, T. C., Chiba, M., et al. 2010, ApJ, 712, 692
Carollo, D., & Chiba, M. 2021, ApJ, 908, 191
Carollo, D., Chiba, M., Ishigaki, M., et al. 2019, ApJ, 887, 22
Chiappini, C., Matteucci, F., & Gratton, R. 1997, ApJ, 477, 765
Chiba, M., & Beers, T. C. 2000, AJ, 119, 2843
Cordoni, G., Da Costa, G. S., Yong, D., et al. 2021, MNRAS, 503, 2539
Cui, X.-Q., Zhao, Y.-H., Chu, Y.-Q., et al. 2012, RAA, 12, 1197
Di Matteo, P., Fragkoudi, F., Khoperskov, S., et al. 2019, A&A, 628, A11
Di Matteo, P., Lehnert, M. D., Qu, Y., & van Driel, W. 2011, A&A, 525, L3
Foreman-Mackey, D., Hogg, D. W., Lang, D., & Goodman, J. 2013, PASP, 125, 306
Franchini, M., Morossi, C., Di Marcantonio, P., et al. 2021, AJ, 161, 9
Gaia Collaboration, Brown, A. G. A., Vallenari, A., et al. 2021, A&A, 649, A1
Gilmore, G., & Reid, N. 1983, MNRAS, 202, 1025
Girard, T. M., Korchagin, V. I., Casetti-Dinescu, D. I., et al. 2006, AJ, 132, 1768
Hayden, M. R., Holtzman, J. A., Bovy, J., et al. 2014, AJ, 147, 116
Helmi, A., Babusiaux, C., Koppelman, H. H., et al. 2018, Natur, 563, 85
Ivezić, Z. ˇ, Sesar, B., Jurić, M., et al. 2008, ApJ, 684, 287
Kordopatis, G., Gilmore, G., Wyse, R. F. G., et al. 2013, MNRAS, 436, 3231
Kordopatis, G., Recio-Blanco, A., de Laverny, P., et al. 2011, A&A, 535, A107
Luo, A. L., Zhao, Y.-H., Zhao, G., et al. 2015, RAA, 15, 1095
Miranda, M. S., Pilkington, K., Gibson, B. K., et al. 2016, A&A, 587, A10
Morrison, H. L., Flynn, C., & Freeman, K. C. 1990, AJ, 100, 1191
Naidu, R. P., Conroy, C., Bonaca, A., et al. 2020, ApJ, 901, 48
Norris, J., Bessell, M. S., & Pickles, A. J. 1985, ApJS, 58, 463
Recio-Blanco, A., de Laverny, P., Kordopatis, G., et al. 2014, A&A, 567, A5
Reddy, B. E., & Lambert, D. L. 2008, MNRAS, 391, 95
Reid, M. J., Menten, K. M., Brunthaler, A., et al. 2014, ApJ, 783, 130
Ruchti, G. R., Fulbright, J. P., Wyse, R. F. G., et al. 2010, ApJL, 721, L92
Ruchti, G. R., Fulbright, J. P., Wyse, R. F. G., et al. 2011, ApJ, 737, 9
Ryan, S. G., & Lambert, D. L. 1995, AJ, 109, 2068
Schönrich, R., Binney, J., & Dehnen, W. 2010, MNRAS, 403, 1829
Steinmetz, M., Guiglion, G., McMillan, P. J., et al. 2020a, AJ, 160, 83
Steinmetz, M., Matijevič, G., Enke, H., et al. 2020b, AJ, 160, 82
Tian, H., Liu, C., Wang, Y., et al. 2020, ApJ, 899, 110
Tian, H., Liu, C., Xu, Y., & Xue, X. 2019, ApJ, 871, 184
Twarog, B. A., & Anthony-Twarog, B. J. 1994, AJ, 107, 1371
van der Kruit, P. C., & Freeman, K. C. 2011, ARA&A, 49, 301
Xiang, M., Ting, Y.-S., Rix, H.-W., et al. 2019, ApJS, 245, 34
York, D. G., Adelman, J., Anderson, John E. J., et al. 2000, AJ, 120, 1579